Journal Pre-proofs

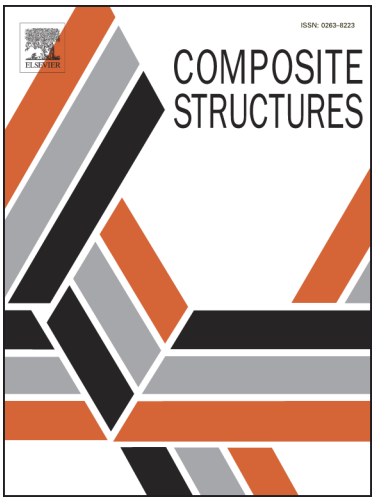

Interlaminar fracture of asymmetrically delaminated specimens: beam modelling and noteworthy characteristics

A.B. de Morais

PII: S0263-8223(21)00206-3
DOI: https://doi.org/10.1016/j.compstruct.2021.113745
Reference: COST 113745

To appear in: *Composite Structures*

Received Date: 16 December 2020
Revised Date: 11 February 2021
Accepted Date: 14 February 2021

Please cite this article as: de Morais, A.B., Interlaminar fracture of asymmetrically delaminated specimens: beam modelling and noteworthy characteristics, *Composite Structures* (2021), doi: https://doi.org/10.1016/j.compstruct.2021.113745

Interlaminar fracture of asymmetrically delaminated specimens: beam modelling and noteworthy characteristics

A. B. de Morais[1,2]

[1]Department of Mechanical Engineering, University of Aveiro, Campus Santiago, 3810-193 Aveiro, Portugal. (Tel.: +351 234 370830; E-mail: abm@ua.pt)

[2]RISCO research centre, Department of Civil Engineering, University of Aveiro, Campus Santiago, 3810-193 Aveiro, Portugal

Abstract

Despite providing interesting mode-mix ratios without elaborate test fixtures, asymmetrically delaminated specimens have been scarcely used for characterizing delamination resistance. This is mostly due to the elaborate analyses employed and the controversy about mode partitioning. This paper presents a beam model for asymmetrically delaminated unidirectional composite specimens. The physical meaning and underlying assumptions of the solutions obtained are clearly identified. Comparison with finite element analyses showed that the present beam model is accurate for a wide range of asymmetry and mode-mix ratios. Since it does not require complicated calculations, the beam model is well-suited for experimental data reduction. Furthermore, traction distributions near the crack-tip were found to differ from those of standard specimens, thereby increasing the interest in studying the fracture behaviour of asymmetrically delaminated specimens.

Keywords: Polymer matrix composites; Fracture mechanics; Delamination; Mixed-mode fracture; Asymmetrically delaminated specimens.

Nomenclature

a Crack length

b Specimen width

$C_{i,j}$ Integration constants (i = 1, 2 and j = 0-3)

D_j Coefficients of a linear differential equation (j = 1-5)

E_1 Longitudinal Young's modulus

E_3 Transverse through-thickness Young's modulus

f_s Timoshenko beam theory transverse shear factor

F_i Transverse load applied to the specimen i-th sub-laminate free-end

G Total strain-energy release rate

G_{13} Transverse through-thickness shear modulus

G_{I} Mode I strain-energy release rate

G_{II} Mode II strain-energy release rate

h Specimen half-thickness

h_i Specimen i-th sub-laminate thickness

I Specimen second moment of area

I_i Specimen i-th sub-laminate second moment of area

K_n Normal cohesive elastic stiffness

K_s Shear cohesive elastic stiffness

L Specimen span

M_i Bending moment on the specimen i-th sub-laminate

M_i Moment applied to the specimen i-th sub-laminate free-end

N Normal force on the specimen sub-laminates

$Q_{i,j}$ Sub-laminate properties and geometry dependent parameters (i = 1,2 and j = 0-3)

t_n Normal cohesive stiffness characteristic thickness

t_s Shear cohesive stiffness characteristic thickness

v_i Vertical displacement of the specimen i-th sub-laminate

$\bar{v}_i$ Vertical displacement of the specimen i-th sub-laminate free-end

$v_{b,i}$ Vertical bending displacement of the specimen i-th sub-laminate

$v_{s,i}$ Vertical transverse shear displacement of the specimen i-th sub-laminate

V_i Transverse shear force on the specimen i-th sub-laminate

δ_n Normal separation

δ_s Shear separation

Δ Normalized vertical displacement of the specimen free-ends

θ_i Cross-section rotation of the specimen i-th sub-laminate

$\bar{\theta}_i$ Cross-section rotation of the specimen i-th sub-laminate free-end

λ_k Elastic traction distribution parameters (k = 1-3)

ν_{13} Longitudinal Poisson's ratio

ν_{23} Transverse Poisson's ratio

σ_c Normal traction

σ_k Normal traction distribution integration constants (k = 1-6)

Σ Dimensionless normal traction

τ_c Shear traction

τ_k Shear traction distribution integration constants (k = 0-6)

τ_k Crack-tip shear traction terms (k = 1-3)

τ_s Transverse shear stress

T Dimensionless shear traction

Abbreviations

ADBM	Asymmetric delamination beam model
ADCB	Asymmetric double cantilever beam
BT	Beam theory
CBT	Corrected beam theory
CFRP	Carbon-fibre reinforced composites
DCB	Double cantilever beam
ELS	End-loaded split
ENF	End-notched flexure
FEA	Finite element analysis
FLDCB	Force-loaded double cantilever beam
FPZ	Fracture process zone
FRMM	Fixed-ratio mixed-mode
GFRP	Glass-fibre reinforced composites
MLDCB	Moment-loaded double cantilever beam
MMB	Mixed-mode bending
SLB	Single-leg bending
UD	Unidirectional
VCCT	Virtual crack closure technique

1. Introduction

Susceptibility to delamination is a well-known weakness of high-performance laminated composites. As a result of extensive research on delamination resistance, several interlaminar fracture test methods were developed and standardized i.e. the double cantilever beam (DCB) for pure mode I (ISO 15024 and ASTM D5528), the end-notched flexure (ENF) for pure mode II (JIS K 7086 and ASTM D7905), the end-loaded split (ELS) for pure mode II (ISO

15114) and the mixed-mode bending (MMB) for mixed-mode I-II (ASTM D6671). All of those methods involve unidirectional (UD) specimens with initial mid-plane delaminations and have well-established easy-to-apply data reduction schemes. The ASTM D6671 standard MMB specimen, in particular, is able to cover a wide range of mode-mix ratios. However, it does require a specific fixture whose weight needs to be taken into account, thereby posing difficulties to high-rate and fatigue tests.

Asymmetrically delaminated specimens are known to provide mixed-mode I-II with simple test fixtures. However, defining the exact mode-mix ratio has been subject of considerable controversy. The so-called global mode partitioning by Williams [1], which is based on simple assumptions concerning specimen sub-laminate loads and curvatures, soon proved to be unsuited [2,3]. Several mode partitioning approaches have subsequently been developed e.g. [2-10]. Such approaches are designated as 'local', since they consider crack-tip features e.g. forces, moments or stress fields described by stress intensity factors.

The unquestionable importance and challenges of mode partitioning seem to have relegated to a minor role the specimen load-displacement response modelling. Yet, the ability to model accurately the load-displacement response of standard delamination specimens has been the main reason behind the widespread use of beam theory (BT) based data reduction schemes. Furthermore, sound beam models that account for the localised flexibility effects near the crack-tip have been developed [11,12]. In fact, Benatti et al. [12] used the Timoshenko BT kinematics to derive an 'enhanced' beam model for asymmetric double cantilever beam (ADCB) specimens. After calibration of extensional and shear stiffness parameters, their [12] model gave quite accurate predictions for the compliance, total strain-energy release rate G and mode-mix ratios of glass-fibre composites. However, the ADCB specimens analysed in [12] only provided a limited range of mode-mix ratios i.e. G_{II}/G = 0-32%, G_{II} being the mode II strain-energy release rate. Dimitri et al. [13] have recently applied the Benatti et al. [12] formulation to asymmetrically delaminated moment-loaded double cantilever beam (MLDCB) specimens. However, they [13] did not compare the results with finite element analyses (FEA). Moreover, Dimitri et al. [13] employed a numerical solution procedure, while the analytical solution of the fundamental equations is a particularly attractive feature of the Benatti et al. [12] formulation.

This paper revisits the Timoshenko beam modelling of asymmetrically delaminated fracture specimens, and proposes the asymmetric delamination beam model (ADBM) for UD composite specimens. Although the ADBM becomes identical to the model of [12] when

applied to the ADCB specimen in equal terms, there are differences and relevant new results worth remarking:

- a different path was followed to obtain general solutions for the tractions;
- an intrinsic limitation of Timoshenko beam modelling is identified;
- the physical meaning of the solution parameters is discussed, allowing considerable simplifications and solutions for strain-energy release rates based solely on crack-tip forces and moments;
- model predictions are assessed for a wide range of mode-mix ratios, which are well beyond the reach of the ADCB specimen analysed in [12].

In fact, the ADBM is here applied to MLDCB and force-loaded double cantilever beam (FLDCB) specimens (Fig. 1), both able to generate the entire range of mode-mix I-II ratios. Despite requiring elaborate loading fixtures, they have actually been implemented [14,15] for composites or adhesive joints. In the end, it is shown that the ADBM is suitable for analysing interlaminar fracture test results of asymmetrically delaminated UD composite specimens. This work did not aim at developing direct expressions for G similar to the ones currently available for standard specimens. Nevertheless, the ADBM equations are fully closed-form i.e. free from any numerical procedures. Finally, differences seen in the traction distributions near the crack-tip relative to standard specimens are an additional motivation for studying the interlaminar fracture behaviour of asymmetrically delaminated specimens.

2. The asymmetric delamination beam model (ADBM)

2.1. Fundamental equations and assumptions

In the scope of Timoshenko BT, interlaminar fracture specimens (Fig. 1) are modelled as two beams bonded in the undelaminated $a \leq x \leq L$ region. We start by analysing the infinitesimal elements of the upper (1) and lower (2) sub-laminates (Fig. 2) in that region. The cross-sections of such elements are subjected to normal forces N, which must be symmetric in both sub-laminates, transverse shear forces V_i, as well as bending moments M_i. The normal σ_c and shear τ_c tractions act on the bonded surfaces. The present sign convention takes as positive the forces, moments and tractions depicted in Fig. 2. The horizontal force, vertical force and moment equilibrium equations are thus

$$\frac{dN}{dx} = b\tau_c \tag{1}$$

$$\frac{dV_1}{dx} = -\frac{dV_2}{dx} = -b\sigma_c \tag{2}$$

$$V_i = \frac{dM_i}{dx} + \frac{bh_i\tau_c}{2} \tag{3}$$

respectively, where b is the specimen width. The two latter equations can be combined into

$$\frac{d^2M_1}{dx^2} = -\frac{bh_1 d\tau_c}{2\ dx} - b\sigma_c,\ \frac{d^2M_2}{dx^2} = -\frac{bh_2 d\tau_c}{2\ dx} + b\sigma_c \tag{4}$$

which are convenient for subsequent derivations.

The bending moments are related to the curvature through the BT fundamental relation

$$M_i = E_1 I_i \frac{d^2 v_{b,i}}{dx^2} \tag{5}$$

where E_1 is the laminate longitudinal Young's modulus, $I_i = bh_i^3/12$ the i-th sub-laminate second moment of area and $v_{b,i}$ the vertical bending displacement.

Assuming linear elasticity, the tractions can be expressed as

$$\sigma_c = K_n\delta_n,\ \tau_c = K_s\delta_s \tag{6}$$

where K_n and K_s are the normal and shear cohesive elastic stiffnesses, respectively, and δ_n and δ_s are the corresponding normal and shear separations. In the scope of beam modelling, the separations are set equal to the bonded surface relative displacements, and thus

$$\delta_n = v_1 - v_2 \tag{7}$$

with the vertical displacements

$$v_i = v_{b,i} + v_{s,i} \tag{8}$$

$v_{s,i}$ being the transverse shear displacement.

Timoshenko BT determines transverse shear displacements through the relation

$$\frac{dv_{s,i}}{dx} = -\frac{V_i}{f_s bh_i G_{13}} \tag{9}$$

where G_{13} is the laminate longitudinal through-thickness shear modulus and $f_s = 5/6$ is the transverse shear factor for rectangular cross-sections. Actually, application of Eq. (9) bears a simplification that has not been remarked: it was developed from energy methods for the parabolic transverse shear stress distribution

$$\tau_s = \frac{3V}{4bh}\left[1 - \left(\frac{y}{h}\right)^2\right] \tag{10}$$

that exists in b-wide and $2h$-thick rectangular cross-section beams [16]. In particular, Eq. (10) ensures that $\tau_s = 0$ at the beam $y = \pm h$ surfaces, which is clearly not the case of the sub-laminates bonded surfaces. Obviously, τ_s-distributions in each sub-laminate depend on both V_i and τ_c. Using the classical mechanics of materials approach [16], it can be shown that

$$\frac{dv_{s,i}}{dx} = -\frac{V_i - \frac{bh_i\tau_c}{6} + \frac{(bh_i\tau_c)^2}{9V_i}}{f_s bh_i G_{13}} \tag{11}$$

However, adopting this more accurate formulation would ultimately lead to non-linear differential equations whose complexity compromises the practical usefulness of beam modelling altogether. It is worth remarking that this issue does not arise for symmetric sub-laminates i.e. $h_1 = h_2 = h$ (Fig. 1); it is easily shown that Eq. (9) is exact, although the τ_s-distribution is different from Eq. (10). The errors of Eq. (9) may in turn become significant for $h_2 >> h_1$, especially because of the high relevance of τ_c in the crack-tip vicinity. Nevertheless, the load-displacement response of beam-like interlaminar fracture specimens is clearly dominated by the bending moments. Moreover, testing specimens with very high h_2/h_1 is not feasible, given the strong susceptibility to large displacements and to premature failure of the thinner sub-laminate. Therefore, as seen below, it is worth keeping Eq. (9).

As for the shear separation, it depends on the bending cross-section rotations of each sub-laminate, which can be set equal to $dv_{b,i}/dx$ in the geometrically linear regime, and on the uniform cross-section displacements caused by N (Fig. 3). Adopting the $\delta_s \geq 0$, $N \geq 0$ and $dv_{b,i}/dx \leq 0$ sign conventions and an appropriate $x_0 > a$ reference position, we have

$$\delta_s(x) - \delta_s(x_0) = \frac{h_1}{2}\left[\left.\frac{dv_{b,1}}{dx}\right|_{x_0} - \left.\frac{dv_{b,1}}{dx}\right|_{x}\right] + \frac{h_2}{2}\left[\left.\frac{dv_{b,2}}{dx}\right|_{x_0} - \left.\frac{dv_{b,2}}{dx}\right|_{x}\right] + \left(\frac{1}{h_1} + \frac{1}{h_2}\right)\int_{x_0}^{x} \frac{N}{Eb} dx \tag{12}$$

Finally, having taken the separations from Timoshenko BT kinematics, it is essential to choose K_n and K_s that are able to model the localised crack-tip effects. This is done by expressing the cohesive elastic stiffnesses as

$$K_n = \frac{E_3}{t_n}, K_s = \frac{G_{13}}{t_s} \tag{13}$$

where E_3 is the through-thickness transverse Young's modulus, while t_n and t_s are characteristic thicknesses whose values have to be calibrated by FEA. Given the approximations inherent to beam modelling, one can not expect t_n and t_s to be independent of material properties and some laminate dimensions. Studies on beam modelling of mode I and mode II delamination in standard symmetrically delaminated specimens have indeed shown small sensitivity of t_n and t_s to materials properties and laminate total thickness [17,18]. The aforementioned approximate treatment of the transverse shear effect was also expected to make t_n and t_s somewhat dependent on h_2/h_1. However, such dependence should be mild enough for safeguarding the overall suitability of beam modelling.

2.2. Solutions for the tractions

Benatti et al. [12] showed that, when applied to the ADCB specimen, the above fundamental beam modelling equations lead to a single 6th-order linear homogeneous differential equation

for σ_c, whose characteristic polynomial has 6 real roots. The solution for σ_c was therefore expressed as the sum of 6 exponential functions multiplied by 6 integration constants. In the end, the latter were determined by solving a final system of 6 linear equations [12]. Intermediate developments did involve more 13 integration constants, but they were shown to be either null or functions of the original 6 integration constants.

In this work we pursue a different less complex route which begins by substituting τ_c/K_s for δ_s in Eq. (12) and performing a triple differentiation. Using Eq. (1), the term involving N is expressed as a function of $d\tau_c/dx$, while the terms on $d^4v_{b,i}/dx^4$ can be written as functions of $d\tau_c/dx$ and σ_c owing to Eqs. (4) and (5). The result of these developments is simply

$$\sigma_c = \left[\frac{E_1 h_1^2 h_2^2}{6K_s(h_2^2 - h_1^2)}\right]\frac{d^3\tau_c}{dx^3} - \left[\frac{2h_1 h_2}{3(h_2 - h_1)}\right]\frac{d\tau_c}{dx} \tag{14}$$

We can now substitute Eq. (14) for σ_c in Eqs. (4) to obtain

$$\frac{d^2M_i}{dx^2} = Q_{i,3}\frac{d^3\tau_c}{dx^3} + Q_{i,1}\frac{d\tau_c}{dx} \tag{15}$$

where

$$Q_{1,3} = -Q_{2,3} = -\frac{E_1 b h_1^2 h_2^2}{6K_s(h_2^2 - h_1^2)} \tag{16}$$

$$Q_{1,1} = \frac{bh_1(3h_1 + h_2)}{6(h_2 - h_1)},\ Q_{2,1} = -\frac{bh_2(h_1 + 3h_2)}{6(h_2 - h_1)} \tag{17}$$

Yet, σ_c is also given by Eq. (6), in which Eqs. (7)-(9) are to be used for expressing δ_n as a function of $v_{b,i}$ and $v_{s,i}$. Successive differentiation leads to

$$\frac{1}{K_n}\frac{d^4\sigma_c}{dx^4} = \frac{1}{E_1}\left(\frac{1}{I_1}\frac{d^2M_1}{dx^2} - \frac{1}{I_2}\frac{d^2M_2}{dx^2}\right) + \frac{6}{5G_{13}b}\left(\frac{1}{h_2}\frac{d^4M_2}{dx^4} - \frac{1}{h_1}\frac{d^4M_1}{dx^4}\right) \tag{18}$$

One can now substitute Eq. (14) for σ_c and Eqs. (15) for the M_i-derivatives in order to arrive at the 7th-order linear homogeneous differential equation

$$\frac{d^7\tau_c}{dx^7} + D_5\frac{d^5\tau_c}{dx^5} + D_3\frac{d^3\tau_c}{dx^3} + D_1\frac{d\tau_c}{dx} = 0 \tag{19}$$

whose coefficients are

$$D_1 = -\frac{12K_nK_s}{E_1^2}\left(\frac{h_1 + h_2}{h_1 h_2}\right)^4 \tag{20}$$

$$D_3 = \frac{12K_n(h_1^3 + h_2^3)}{E_1 h_1^3 h_2^3} + \frac{24K_nK_s}{5E_1G_{13}}\left(\frac{h_1 + h_2}{h_1 h_2}\right)^2 \tag{21}$$

$$D_5 = -\frac{h_1 + h_2}{h_1 h_2}\left(\frac{4K_s}{E_1} + \frac{6K_n}{5G_{13}}\right) \tag{22}$$

The solution of Eq. (19) demands finding the 7 roots of the characteristic polynomial on λ

$$\lambda\left(\lambda^6 + D_5\lambda^4 + D_3\lambda^2 + D_1\right) = 0 \tag{23}$$

one of which is, obviously, $\lambda = 0$. Benatti et al. [12] did not remark that the remaining 6 roots

are easy to compute, as the 6th-order polynomial of Eq. (23) can be converted into a 3rd-order polynomial on λ^2. Closed-form solutions are available for the roots of 3rd-order polynomials. Owing to the typical laminate properties and thicknesses, Eq. (23) has 3 pairs of real $\pm\lambda_i$ roots. Therefore, the solution of Eq. (19) can be written as

$$\tau_c = \tau_0 + \sum_{k=1}^{3}[\tau_k \exp(-\lambda_k x) + \tau_{k+3}\exp(\lambda_k x)] \tag{24}$$

where τ_k are integration constants. The substitution of Eq. (24) for τ_c in Eq. (14) yields the solution for σ_c that can be expressed as

$$\sigma_c = \sum_{k=1}^{3}[\sigma_k \exp(-\lambda_k x) + \sigma_{k+3}\exp(\lambda_k x)] \tag{25}$$

with σ_k being integration constants that are, obviously, related to τ_k. The present general solution is thus identical to the one obtained in [12].

It can be shown that this formulation reduces to the beam models of [18,19] for mode I and mode II fracture of symmetrically delaminated specimens i.e. $h_1 = h_2 = h$ (Fig. 1). This case involves decoupled 3rd-order and 4th-order linear differential equations for τ_c and σ_c, respectively, whose solutions are

$$\tau_c = \tau_0 + \tau_2 \exp(-\lambda_2 x) + \tau_5 \exp(\lambda_2 x) \tag{26}$$

$$\sigma_c = \sigma_1 \exp(-\lambda_1 x) + \sigma_3 \exp(-\lambda_3 x) + \sigma_4 \exp(\lambda_1 x) + \sigma_6 \exp(\lambda_3 x) \tag{27}$$

Though used subsequently for traction distributions comparison purposes, the symmetrically delaminated case is not developed here.

2.3. Physical interpretation and scope of the solutions

Before proceeding to the main model results, it is important to analyse the physical meaning of the above solutions by taking the MLDCB and FLDCB specimens as basis for discussion. In general mixed-mode I-II cases, both σ_c and τ_c attain peak values at the $x = a$ crack-tip position (Fig. 1). It should be noted that beam modelling suppresses the crack-tip singularity. As we move away from the crack-tip within the undelaminated region, σ_c and τ_c gradually decrease. If the $x = L$ built-in cross-section (Fig. 1) is sufficiently distant from the crack-tip, σ_c and τ_c should become consistent with the whole laminate beam response i.e. $\sigma_c = 0$ and τ_c must be equal to $\tau_s(y = h_2 - h)$ (Fig. 1) given by Eq. (10). Finally, as we get near the $x = L$ built-in cross-section, σ_c and τ_c undergo further changes. Therefore, near the $x = a$ crack-tip position the terms of Eqs. (24) and (25) on $\exp(-\lambda_k x)$ play a major role, while those on $\exp(\lambda_k x)$ are negligible. The latter terms in turn become relevant near the $x = L$ built-in cross-section. However, modelling the built-in effects can already be done with simpler beam models for

symmetric sub-laminates e.g. adapting to the MLDCB and FLDCB specimens the models developed in [18,19].

Where the mode I component is concerned, the typical properties and thicknesses of UD composite specimens lead to λ_1 and λ_3 (see Eq. (27)) values that cause a very steep σ_c-decrease from the crack-tip peak value [18,20]. Therefore, any σ_c-surge can only occur in a very small region near the built-in end and have a negligible effect on the overall specimen response.

Regarding the mode II component, it is well-known that the τ_c-decrease from the crack-tip peak value to τ_s predicted by Eq. (10) takes place along a much longer distance than in mode I loadings [17,19,20]. This gives rise to the long fracture process zones (FPZ) typical of mode II delamination. As we approach the $x = L$ cross-section (Fig. 1), $\tau_c = \tau_s$ given by Eq. (10) must gradually decline to $\tau_c = 0$ for an ideal built-in end. Actually, a similar τ_c-distribution exists in the $a \leq x \leq L$ region of the ENF specimen, for which $x = L$ is the half-span where the load acts. In fact, there is a shear force reversal at the load-point position which makes $\tau_c(L) \approx 0$ [19]. The effect of this τ_c-decrease, which is associated with the term on $\exp(\lambda_2 x)$ of Eq. (26), proved to be relevant only when the FPZ gets close to the ENF specimen load-point [19]. This situation should be avoided in actual delamination resistance tests, as it leads to artificially high perceived toughness values [19].

Therefore, it is reasonable to considered here:

- only cases in which the crack-tip is sufficiently distant from the built-in end of MLDCB and FLDCB specimens (Fig. 1);
- that the built-in end local perturbations of the traction distributions do not affect significantly the specimen load-displacement response and strain-energy release rate evaluation.

This framework greatly simplifies the analysis by allowing the solutions for the tractions to be expressed as

$$\tau_c \approx \tau_0 + \sum_{k=1}^{3} \tau_k \exp(-\lambda_k x) \tag{28}$$

$$\sigma_c \approx \sum_{k=1}^{3} \sigma_k \exp(-\lambda_k x) \tag{29}$$

where, from Eq. (14),

$$\sigma_k = \left[\frac{2h_1 h_2 \lambda_k}{3(h_2 - h_1)} - \frac{E_1 h_1^2 h_2^2 \lambda_k^3}{6K_s(h_2^2 - h_1^2)} \right] \tau_k \tag{30}$$

It should be noted that a similar discarding of exponential terms was done by Qiao and Wang [11], whose solutions Benatti et al. [12] criticized for being merely approximate. However, as discussed above and confirmed by the results presented below, neglecting those terms is

adequate for composite interlaminar fracture specimens.

Finally, it is worth remarking that the next developments assume:

- load combinations which do not promote contact between the delaminated surfaces;
- ideal built-in ends, which, obviously, cannot be attained.

In practice, a portion of the specimen is clamped, as in the ELS specimen. Application of BT based data reduction schemes only requires considering an increased 'corrected' span determined experimentally [21].

2.4. Strain-energy release rate components

At this stage, one may substitute Eq. (28) for τ_c in Eqs. (15) and perform a double integration that yields

$$M_i = -\sum_{k=1}^{3}\tau_k \exp(-\lambda_k x)\left(\lambda_k Q_{i,3} + \frac{Q_{i,1}}{\lambda_k}\right) + (Q_{i,1}\tau_0 + C_{i,3})x + C_{i,2} \tag{31}$$

introducing the $C_{i,3}$ and $C_{i,2}$ integration constants. Eq. (28) should also be substituted for τ_c in Eq. (1), whose integration provides the normal force

$$\frac{N}{b} = \tau_0(x-a) - \sum_{k=1}^{3}\tau_k\left[\frac{\exp(-\lambda_k x) - \exp(-\lambda_k a)}{\lambda_k}\right] \tag{32}$$

after imposing that $N(a) = 0$. It is now necessary to use the equations that result from a first and a second differentiation of Eq. (12). By noting that $d^2v_{b,i}/dx^2$ are given by Eqs. (5) after substituting Eq. (31) for M_i, we get

$$C_{1,3} = -\frac{b\tau_0 h_1(h_1+h_2)^2}{6h_2(h_2-h_1)},\ C_{2,3} = \frac{b\tau_0 h_2(h_1+h_2)^2}{6h_1(h_2-h_1)} \tag{33}$$

$$C_{1,2} = \frac{bh_1^2}{6h_2}\left(\sum_{k=1}^{3}\left[\frac{\tau_k \exp(-\lambda_k a)}{\lambda_k}\right] - \tau_0 a\right),\ C_{2,2} = \frac{bh_2^2}{6h_1}\left(\sum_{k=1}^{3}\left[\frac{\tau_k \exp(-\lambda_k a)}{\lambda_k}\right] - \tau_0 a\right) \tag{34}$$

It is also useful to substitute Eq. (28) for τ_c and Eq. (31) for M_i in Eqs. (3) in order to obtain

$$V_i = \sum_{k=1}^{3}\tau_k \exp(-\lambda_k x)\left(\lambda_k^2 Q_{i,3} + Q_{i,1} + \frac{bh_i}{2}\right) + \left(Q_{i,1} + \frac{bh_i}{2}\right)\tau_0 + C_{i,3} \tag{35}$$

Finally, τ_k (k = 0-3) can be determined from the sub-laminate crack-tip section transverse shear forces and bending moments. The latter can be written generally for both the MLDCB and FLDCB specimens (Fig. 1) as

$$V_i(a) = F_i,\ M_i(a) = \overline{M}_i + F_i a \tag{36}$$

Actually, it is convenient to impose first

$$V_1(a) + V_2(a) = F_1 + F_2 \tag{37}$$

as this leads directly to

$$\tau_0 = \frac{6h_1h_2(F_1+F_2)}{b(h_1+h_2)^3} \tag{38}$$

which does coincide with the transverse shear stress $\tau_s(y = h_2 - h)$ (Fig. 1) predicted by Eq. (10). Therefore, as discussed in Section 2.3, as we move away from the crack-tip within the specimen undelaminated region, the terms on $\exp(-\lambda_k x)$ of Eq. (28) become negligible and $\tau_c \approx \tau_0$ is consistent with the whole laminate beam response. The remaining integration constants can be obtained from the system formed by the following 3 linear equations:

$$\sum_{k=1}^{3} \overline{\tau}_k \left[\frac{2(h_1+h_2)}{3} - \lambda_k^2 \frac{E_1 h_1 h_2}{6K_s} \right] = \frac{h_2^2 F_1 + h_1^2 F_2}{b h_1 h_2} - \frac{2(h_1+h_2)}{3}\tau_0 \tag{39}$$

$$\sum_{k=1}^{3} \overline{\tau}_k \left[\frac{\lambda_k E_1 h_1^2 h_2^2}{6K_s(h_1+h_2)} + \frac{(h_1+h_2)^2}{6\lambda_k} \right] = \frac{h_2 M_1(a) + h_1 M_2(a)}{b} \tag{40}$$

$$\sum_{k=1}^{3} \overline{\tau}_k \frac{\lambda_k E_1 h_1 h_2}{6K_s} = \frac{h_2^2 M_1(a) + h_1^2 M_2(a)}{b h_1 h_2} \tag{41}$$

written in terms of the crack-tip shear traction terms

$$\overline{\tau}_k = \tau_k \exp(-\lambda_k a) \tag{42}$$

Finally, one can compute successively σ_k (k = 1-3), $\tau_c(a)$ and $\sigma_c(a)$ from Eqs. (28)-(30), and, because of Eqs. (6),

$$G_{\mathrm{I}} = \frac{\sigma_c^2(a)}{2K_n},\ G_{\mathrm{II}} = \frac{\tau_c^2(a)}{2K_s} \tag{43}$$

Therefore, the physical interpretation and scope of the solutions obtained do support the 'local' mode partitioning approaches based on crack-tip forces and moments that have received so much attention in the literature (see Section 1).

2.5. Moment-rotation and load-displacement responses

The moment-rotation and load-displacement responses are a basic result of MLDCB and FLDCB tests. In the geometrically linear regime adopted, the beam cross-section rotations in each specimen sub-laminate are $\theta_i \approx dv_{b,i}/dx$. The successive integration of Eqs. (5) after substituting Eqs. (31) for M_i yields

$$E_1 I_i \theta_i = \sum_{k=1}^{3} \tau_k \exp(-\lambda_k x)\left(Q_{i,3} + \frac{Q_{i,1}}{\lambda_k^2}\right) + (Q_{i,1}\tau_0 + C_{i,3})\frac{x^2}{2} + C_{i,2}x + C_{i,1} \tag{44}$$

$$E_1 I_i v_{b,i} = -\sum_{k=1}^{3} \tau_k \exp(-\lambda_k x)\left(\frac{Q_{i,3}}{\lambda_k} + \frac{Q_{i,1}}{\lambda_k^3}\right) + (Q_{i,1}\tau_0 + C_{i,3})\frac{x^3}{6} + C_{i,2}\frac{x^2}{2} + C_{i,1}x + C_{i,0} \tag{45}$$

The new $C_{i,1}$ and $C_{i,0}$ integration constants are easily determined from the $\theta_i(L) = 0$ and $v_{b,i}(L) = 0$ boundary conditions (Fig. 1), especially because the terms on $\tau_k \exp(-\lambda_k L)$ are negligible. As for the transverse shear contribution, one must substitute Eqs. (35) for V_i in Eqs. (9), integrate and impose that $v_{s,i}(L) = 0$ to obtain

$$\frac{5G_{13}bh_i}{6} v_{s,i} = \sum_{k=1}^{3} \tau_k \exp(-\lambda_k x)\left(\frac{2\lambda_k^2 Q_{i,3} + 2Q_{i,1} + bh_i}{2\lambda_k}\right) + \left[\left(Q_{i,1} + \frac{bh_i}{2}\right)\tau_0 + C_{i,3}\right](L - x) \tag{46}$$

Evidently, it is necessary to add the response of the sub-laminates $0 \leq x \leq a$ region (Fig. 1), which is straightforward in the scope of Timoshenko BT. For the MLDCB specimen (Fig. 1), one is interested in the $\overline{M}_i$ - $\overline{\theta}_i$ response, where

$$\overline{\theta}_i = \theta_i(0) = \theta_i(a) - \frac{\overline{M}_i a}{E_1 I_i} \tag{47}$$

and thus from Eqs. (42) and (44) and the specimen boundary conditions,

$$E_1 I_i \overline{\theta}_i = \sum_{k=1}^{3} \overline{\tau}_k \left(Q_{i,3} + \frac{Q_{i,1}}{\lambda_k^2} \right) + (Q_{i,1}\tau_0 + C_{i,3}) \frac{a^2 - L^2}{2} + C_{i,2}(a - L) - \overline{M}_i a \tag{48}$$

In turn, for the FLDCB specimen the response of interest is the $\overline{F}_i$ - $\overline{v}_i$ one, where

$$\overline{v}_i = v_i(0) = v_i(a) - \theta_i(a)a + \frac{F_i a^3}{3E_1 I_i} + \frac{6F_i a}{5G_{13} b h_i} \tag{49}$$

and $v_i(a)$ and $\theta_i(a)$ can be obtained from Eqs. (42), (44)-(46). This leads to

$$\begin{aligned} \overline{v}_i = \sum_{k=1}^{3} \overline{\tau}_k \left[-\left(Q_{i,3} + \frac{Q_{i,1}}{\lambda_k^2} \right) \frac{1 + \lambda_k a}{E_1 I_i \lambda_k} + \frac{3\left(2\lambda_k^2 Q_{i,3} + 2Q_{i,1} + b h_i\right)}{5G_{13} b h_i \lambda_k} \right] + \frac{3\tau_0 (L - a)}{5G_{13}} \\ + (Q_{i,1}\tau_0 + C_{i,3}) \left[\frac{L^3 - a^3}{E_1 I_i} + \frac{6(L - a)}{5G_{13} b h_i} \right] + \frac{3C_{i,2}(L^2 - a^2) + 2F_i a^3}{6E_1 I_i} + \frac{6F_i a}{5G_{13} b h_i} \end{aligned} \tag{50}$$

3. Results and discussion

3.1. Cohesive stiffness characteristic thickness values

The two sets of material properties here employed are meant to represent the most recent generation of UD high-strength carbon fibre reinforced composites (CFRP) and the traditional glass-fibre reinforced composites (GFRP). For the former case, the properties used were E_1 = 180 GPa, E_3 = 10 GPa, G_{13} = 5.5 GPa, longitudinal Poisson's ratio ν_{13} = 0.3 and transverse Poisson's ratio ν_{23} = 0.42. As for the GFRP, E_1 = 40 GPa, E_3 = 10 GPa, G_{13} = 3.5 GPa, ν_{13} = 0.3 and ν_{23} = 0.45 were assumed. The specimen dimensions were (Fig. 1) $2h$ = 6 mm, L = 120 mm and a = 50 mm. Such dimensions can be compared to the ISO 15114 recommendations for the ELS specimen, which has a similar built-in end: $2h$ = 3 mm for CFRP, $2h$ = 5 mm for GFRP, both with 60% fibre volume content, L = 100 mm and a > 50 mm. Therefore, the present specimens have higher h/a, and thus an enhanced transverse shear contribution. This is especially the case of CFRP specimens, whose higher E_1/G_{13} makes them far more sensitive to transverse shear. The importance of adopting such geometries derives from the ADBM limitations in dealing with transverse shear seen above. The transverse shear effect in the present CFRP specimens is also significantly higher in the undelaminated region, due to the larger $h/(L-a)$. Furthermore, the transverse shear effect is even higher in the thicker sub-laminate of asymmetrically delaminated specimens.

Results are here presented for h_2/h_1 = 1.5, 3 and 5 under several M_2/M_1 and F_2/F_1 ratios

(Fig. 1) providing a wide range of G_{II}/G ratios. As the $h_2/h_1 > 1$ configuration was adopted, the loadings imposed always involved clockwise M_1 and upward F_1 (Fig. 1), here taken as positive. In turn, especially for mode I dominated cases, anti-clockwise M_2 and downward F_2 loadings were applied, here taken as negative. The ADBM predictions were compared to FEA conducted with the Abaqus® code. The numerical models were constructed with two-dimensional 8-node solid quadratic reduced integration elements. Plane stress and material transverse isotropy were assumed. The loadings imposed were small enough to avoid large displacements. G_I and G_{II} were computed by the virtual crack closure technique (VCCT).

As discussed in Section 2.1, the first issue to be addressed concerned the K_n and K_s cohesive elastic stiffnesses Eq. (13). The optimal values of t_n and t_s were determined for each set of material properties and h_2/h_1 ratio by minimizing the $\{[G_I(\text{ADBM})-G_I(\text{FEA})]^2 + [G_{II}(\text{ADBM})-G_{II}(\text{FEA})]^2\}$ residual calculated for the FLDCB specimen. As expected from previous studies [17,18], t_n and t_s were not significantly affected by the highly different material properties here considered (Fig. 4), manifested in the wide gap of E_3/E_1 and G_{13}/E_1. Although t_n became more sensitive to material properties for higher h_2/h_1, the overall variability of t_n and t_s is clearly mild, thereby confirming the interest in beam modelling.

3.2. Strain-energy release rate and mode-mix

The t_n and t_s values determined above enabled the ADBM predictions for the mode-mix (Figs. 5-7) and G (Figs. 8-10) to be in excellent agreement with FEA results. All results of Figs. 8-10 were normalized by the BT prediction [1]

$$G = \frac{1}{2bE_1}\left\{\frac{M_1^2(a)}{I_1} + \frac{M_2^2(a)}{I_2} - \frac{[M_1(a)+M_2(a)]^2}{I}\right\} \tag{51}$$

where I is the specimen second moment of area. It must be mentioned that no results are plotted for the MLDCB specimen, for which $M_i(a) = M_i$, because, as expected, both ADBM and FEA gave results identical to Eq. (51). Actually, Figs. 5-10 confirm that G_I and G_{II} in beam-like specimens are clearly dominated by crack-tip bending moments. The minor role of transverse shear is certainly a key factor for the good results of beam modelling, given the approximate way transverse shear is dealt with (see Section 2.1). In fact, the maximum error attained in G for the higher $h_2/h_1 = 5$ (Fig. 10) was only 0.6 %. Evidently, the normalized $G > 1$ seen in Figs. 8-10 result from the crack-tip section rotations and displacements which are responsible for the well-known crack length corrections in corrected beam theory (CBT). As in standard symmetrically delaminated specimens [17-20], such corrections are larger for: the mode I component, hence the higher normalized G for the $F_2/F_1 < 0$ cases (Figs. 8-10); the

more anisotropic CFRP specimens, which have notably lower E_3/E_1 and G_{13}/E_1.

3.3. Moment-rotation and load-displacement responses

The ADBM predicts the MLDCB specimen end-rotations $\overline{\theta}_i$ and FLDCB specimen vertical end-displacements $\overline{v}_i$ that would be measured in actual experiments. The results presented below are restricted to the latter, as the ADBM errors were higher. This is easily understood considering BT predictions for the absolute values of $\overline{\theta}_i$ and $\overline{v}_i$, which are, respectively,

$$|\overline{\theta}_i|_{BT} = \left|\frac{(\overline{M}_1 + \overline{M}_2)(a-L)}{E_1 I} - \frac{\overline{M}_i a}{E_1 I_i}\right| \tag{52}$$

$$|\overline{v}_i|_{BT} = \left|\frac{(F_1 + F_2)(L^3 - a^3)}{3E_1 I} + \frac{F_i a^3}{3E_1 I_i}\right| \tag{53}$$

As in CBT of symmetrically delaminated specimens, the effects of crack-tip rotation and deflection give rise to an augmented crack length to which $\overline{v}_i$ is much more sensitive than $\overline{\theta}_i$, given the cubic power of a. The results plotted in Fig. 11-13 for the normalized vertical end-displacements

$$\Delta = \frac{|\overline{v}_1| + |\overline{v}_2|}{|\overline{v}_1|_{BT} + |\overline{v}_2|_{BT}} \tag{54}$$

show the ADBM very good accuracy, even though t_n and t_s were optimized for fitting the strain-energy release rates. In fact, the largest differences between the ADBM and FEA seen in the narrow scale of Fig. 13 are under 1.5%.

3.4. Notes on further assessment

The ADBM was also evaluated for MLDCB and FLDCB specimens with larger a = 80 mm crack length. The other specimen dimensions, material properties, cohesive stiffness characteristic thicknesses (t_n and t_s) and load ratios applied were identical to those adopted in the previous sections. The results obtained were very similar to the ones presented above, and thus are here omitted. As expected, the larger crack length increased the dominance of crack-tip bending moments, which made the mode-mix ratios of FLDCB and MLDCB specimens get even closer. Furthermore, the reduced $(L - a)$ crack-tip distance to the built-in end (Fig. 1) did not affect the ADBM accuracy, thereby showing that discarding the terms on $\exp(\lambda_k x)$ of the general solutions for τ_c (Eq. 24) and σ_c (Eq. 25) is an adequate approximation.

Asymmetrically delaminated UD composite specimens have been scarcely used for characterising delamination resistance [22,23]. The experimental study by Ducept et al. [22] is of particular interest here, because its results were analysed in [12], thus allowing the

comparison between the ADBM and the 'enhanced' BT. The UD E-glass/epoxy ADCB specimen dimensions (Fig. 14) were $2h$ = 5 mm, a = 35 mm, L = 150 mm, b = 20 mm and had h_1/h_2 = 1, 0.778, 0.6, 0.455, 0.333 and 0.231. The elastic moduli used in [12] were E_1 = 25.7 GPa, E_3 = 6.5 GPa and G_{13} = 2.5 GPa. It is worth noting the low E_1 because the specimens were manufactured by hand lay-up [22]. For an accurate comparison with the formulation of [12], the cohesive stiffness characteristic thicknesses were set equal to those there adopted i.e. $t_n = 2h/6.9$ and $t_s = 2h/16.2$. In these circumstances, the ADBM results were identical to those of the 'enhanced' BT [12], except for the h_1/h_2 = 0.231 specimen, which gives rise to complex roots for the base differential Eq. (19) solution. This case was not considered here, because it is not representative of typical material properties and specimen geometries of high performance CFRP or GFRP.

4. On the interest in testing asymmetrically delaminated specimens

The above results show that the ADBM provides a suitable framework for analysing the interlaminar fracture test results of asymmetrically delaminated UD composite specimens. Besides the demonstrated accuracy, the ADBM only involves closed-form solutions i.e. no numerical iterative calculation procedures are needed. Therefore, it can be easily implemented in standard spreadsheets. Moreover, cohesive stiffness characteristic thickness values can be provided for the typical range of material properties and sub-laminate thickness ratios. One can even envisage the future development of:

- closed-form solutions similar to CBT for simple specimens such as the ADCB;
- effective crack based data analysis methods [21] that are able to deal with the large FPZ associated to the mode II component.

However, the practical usefulness of testing asymmetrically delaminated specimens can be questioned, especially because the standard MMB specimen covers a wide range of mixed-mode I-II combinations. Moreover, the MMB test fixture is not excessively complicated, although it does have some relevant drawbacks: the weight of fixture needs to be taken into account in toughness measurements [24] and poses difficulties for fatigue and high-rate testing. The MLDCB and FLDCB are even more versatile, allowing pure mode I and mode II tests, but they do require more complex loading systems.

A possible advantage of asymmetrically delaminated specimens could be to achieve a considerable range of mixed-mode I-II combinations with simple test fixtures, The ADBM shows that G_{II}/G is barely above 30% for ADCB specimens (Fig. 14) with h_2/h_1 = 5, which is

a degree of asymmetry already susceptible to large displacements and premature failure of the thinner sub-laminate. Nonetheless, the ADCB specimen (Fig. 14) with $h_2/h_1 = 3$ provides the interesting $G_{II}/G \approx 23\%$ ratio, for which the MMB test setup requires longer lever arms [24].

The fixed-ratio mixed mode (FRMM) [25] (Fig. 15) and the single-leg bending (SLB) [26] (Fig. 16) can also be applied to asymmetrically delaminated specimens. Besides promoting higher G_{II}/G, the position of the thicker sub-laminate depicted in Figs. 15 and 16 is able to avoid premature bending failure of the thinner sub-laminate and large displacement. The $G_{II}/G \approx 53\%$ for $h_1/h_2 = 5$ is, again, an interesting mode-mix ratio for characterizing the mixed-mode I-II fracture envelope, representing a non-negligible increase from the $G_{II}/G \approx 40\%$ of symmetrically delaminated specimens. However, unless new simple tests are developed, it appears that asymmetric delaminations alone are unable to achieve mode II dominated configurations e.g. $G_{II}/G \approx 75\%$.

Finally, one can profit from the absence of singularity in beam models to probe into the traction distributions in the crack-tip vicinity. In particular, it is interesting to compare the traction distributions of asymmetrically and standard symmetrically delaminated specimens. The level of tractions relative to G can be assessed through the dimensionless tractions $\Sigma = b\sigma_c/G$ and $T = b\tau_c/G$. This exercise is done here for CFRP specimens with the same properties and dimensions considered in the previous sections and $h_2/h_1 = 3$. The first case analysed is the ADCB specimen (Fig. 14), for which the ADBM predicts $G_{II}/G = 22.5\%$. Fig. 17 compares the traction levels with those of a symmetrically delaminated FLDCB specimen (Fig. 1) under the $F_2/F_1 = -5.03$ load ratio that leads to same G_{II}/G ratio. It can be seen that traction levels in the crack-tip vicinity are much higher in the symmetrically delaminated specimen.

The second case analysed is the FRMM specimen (Fig. 15), for which the ADBM predicts $G_{II}/G = 48.5\%$. Fig. 18 compares the traction levels to those of a symmetrically delaminated FLDCB specimen (Fig. 1) under the $F_1/F_2 = 10.8$ that promotes an identical G_{II}/G ratio. In contrast with the previous case, the traction levels in the crack-tip neighbourhood are now much higher for the asymmetrically delaminated specimen.

It is worth noting that, in spite of the different traction levels, the σ_c/τ_c traction ratios are quite similar for both types of specimens (Fig. 19). Furthermore, crack propagation is well-known to involve a previous FPZ build-up stage which implies traction redistributions. In the end, asymmetrically and symmetrically delaminated specimens should have identical fracture toughness values. This was confirmed by Ducept et al. [22], but, as seen above, the ADCB

specimens used provided a narrow range of mode-mix ratios. Yet, the results of Figs. 17 and 18 suggest that asymmetrically and symmetrically delaminated specimens may have different FPZ build-up stages. This issue is particularly relevant in toughened material systems e.g. [27], which develop quite large FPZ. Moreover, asymmetrically delaminated specimens could show a higher sensitivity to FPZ formation. This feature is very favourable for evaluating traction-separation laws using recently proposed methods [19,28]. Therefore, the interlaminar fracture behaviour of asymmetrically delaminated specimens is clearly worth investigating.

5. Conclusions

The present work revisited the Timoshenko beam modelling of asymmetrically delaminated unidirectional composite specimens following a different route to obtain general solutions for the traction distributions. The development of the fundamental equations and the physical interpretation of the solutions provided a first set of conclusions:

- The usual treatment of transverse shear is inconsistent with the tractions near the crack-tip. However, accounting accurately for the transverse shear effect would lead to non-linear differential equations.
- Nevertheless, the traction distributions do tend to the Timoshenko beam theory predictions in regions sufficiently distant from the crack-tip and load or support points.
- The typical elastic properties and geometries of interlaminar fracture specimens allow discarding three terms of the general solutions for the traction distributions. This greatly simplifies data analysis and enables mode partitioning approaches based on crack-tip forces and moments.

The above conclusions found support in the results herein obtained for unidirectional composite moment-loaded and force-loaded double cantilever beam specimens under a wide range of mode-mix I-II ratios. Moreover, the results showed that:

- The errors brought about by the aforementioned deficiency in transverse shear modelling are quite small, given the clearly dominant role of bending moments.
- The cohesive elastic stiffnesses were not too sensitive to the sub-laminate thickness ratio and material properties.
- Owing to the accuracy and simplicity, the present beam model provides an adequate framework for data analysis of interlaminar fracture tests on asymmetrically delaminated specimens;

- Traction distributions in the crack-tip vicinity of asymmetrically delaminated specimens can differ significantly from those of standard symmetrically delaminated ones under the same mode-mix ratio.

Therefore, the interlaminar fracture behaviour of asymmetrically delaminated specimens is clearly worth investigating.

Data Availability

The raw/processed data required to reproduce these findings cannot be shared at this time as the data also forms part of an ongoing study.

References

[1] Williams JG. On the calculation of energy release rates for cracked laminates. Int J Fract 1988;36:101–19.

[2] Schapery RA, Davidson BD. Prediction of energy release rate for mixed-mode delamination using classical plate theory. Appl Mech Rev 1990;43:S281–7.

[3] Suo Z, Hutchinson JW. Interface crack between two elastic layers. Int J Fract 1990;43:1–18.

[4] Bruno D, Greco F. Mixed mode delamination in plates: a refined approach. Int J Solids Struct 2001;38:9149–77.

[5] Zou Z, Reid SR, Soden PD, Li S. Mode separation of energy release rate for delamination in composite laminates using sublaminates. Int J Solids Struct 2001;38:2597–613.

[6] Wang J, Qiao P. Fracture analysis of shear deformable bi-material interface. J Eng Mech 2006;132:306-16.

[7] Luo Q, Tong L. Analytic formulas of energy release rates for delamination using a global–local method. Int J Solids Struct 2012;49:3335–44.

[8] Harvey CM, Wang S. Mixed-mode partition theories for one-dimensional delamination in laminated composite beams. Eng Fract Mech 2012;96:737-59.

[9] Li W, Cheng G, Wang D, Wu J. A mixed mode partition method for delaminated beam structure. Eng Fract Mech 2015;148:15–26.

[10] Valvo PS. On the calculation of energy release rate and mode mixity in delaminated laminated beams. Eng Fract Mech 2016;165:114–39.

[11] Qiao P, Wang J. Novel joint deformation models and their application to delamination

fracture analysis. Compos Sci Technol 2005;65:1826-39.

[12] Bennati S, Colleluori M, Corigliano D, Valvo PS. An enhanced beam-theory model of the asymmetric double cantilever beam (ADCB) test for composite laminates. Compos Sci Technol 2009;69:1735-45.

[13] Dimitri R, Tornabene F, Zavarise G. Analytical and numerical modeling of the mixed-mode delamination process for composite moment-loaded double cantilever beams. Compos Struct 2018;187:535-53.

[14] Sørensen BF, Jørgensen K, Jacobsen TK, Østergaard RC. DCB-specimen loaded with uneven bending moments. Int J Fract 2006;141:163-76.

[15] Singh HK, Chakraborty A, Frazier CE, Dillard DA. Mixed mode fracture testing of adhesively bonded wood specimens using a dual actuator load frame. Holzforschung 2010;64: 353-61.

[16] Timoshenko SP. Strength of materials: elementary theory and problems. Vol. 1, Melbourne (FL), Krieger Publishing, 1984.

[17] de Morais AB. Novel cohesive beam model for the End-Notched Flexure (ENF) specimen. Eng Frac Mech 2011;78:3017-29.

[18] de Morais AB. Mode I cohesive zone model for delamination in composite beams. Eng Fract Mech 2013;109:236-45.

[19] de Morais AB. Evaluation of a trilinear traction-separation law for mode II delamination using the effective crack method. Composites Part A 2019;121:74-83.

[20] de Morais AB. Cohesive zone beam modelling of mixed-mode I-II delamination. Composites Part A 2014;64:124-31.

[21] Blackman BRK, Brunner AJ, Williams JG. Mode II fracture testing of composites: a new look at an old problem. Eng Fract Mech 2006;73:2443-55.

[22] Ducept F, Gamby D, Davies P. A mixed-mode failure criterion derived from tests on symmetric and asymmetric specimens. Compos Sci Technol 1999;59:609-19.

[23] Mollón V, Bonhomme J, Viña J, Argüelles A. Theoretical and experimental analysis of carbon epoxy asymmetric dcb specimens to characterize mixed mode fracture toughness. Polym Test 2010;29:766–70.

[24] Reeder JR. Refinements to the mixed-mode bending test for delamination toughness. J Compos Technol Res 2003;25:191–5.

[25] Kinloch AJ, Wang Y, Williams JG, Yayla P. The mixed-mode delamination of fibre composite materials. Compos Sci Technol 1993;47:225-37.

[26] Davidson BD, Sundararaman V. A single leg bending test for interfacial fracture toughness determination. Int J Fract 1996;78:193–210.

[27] Davidson BD, Kumar M, Soffa MA. Influence of mode ratio and hygrothermal condition on the delamination toughness of a thermoplastic particulate interlayered carbon/epoxy composite. Compos Part A 2009;40:67–79.

[28] Arrese A, Insausti N, Mujika F, Perez-Galmés M, Renart J. A novel experimental procedure to determine the cohesive law in ENF tests. Compos Sci Technol 2019;170:42–50.

Figures

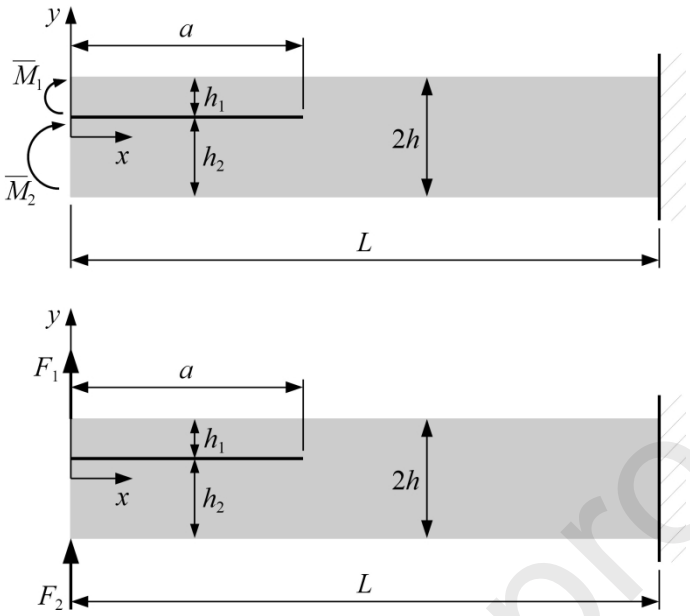

Fig. 1. The MLDCB and FLDCB specimens.

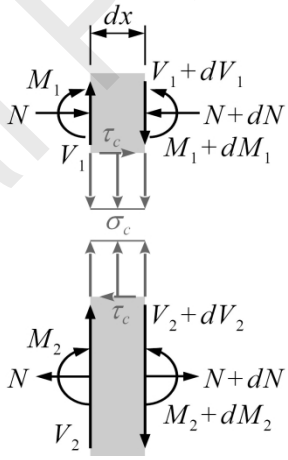

Fig. 2. Forces, moments and tractions acting on infinitesimal elements of the upper (1) and lower (2) sub-laminates in the specimen $a \le x \le L$ region (Fig. 1).

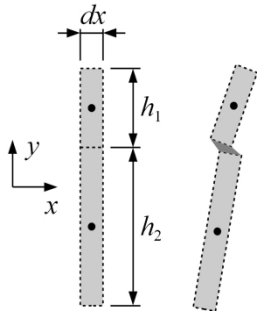

Fig.3. Deformations of sub-laminates infinitesimal elements in the specimen $a \le x \le L$ region (Fig. 1).

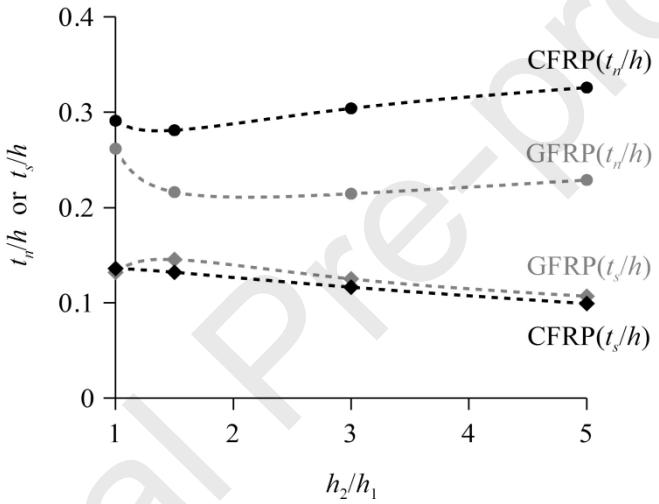

Fig.4. Effect of the sub-laminate thickness ratio (Fig. 1) on the cohesive stiffness characteristic thickness values of the CFRP and GFRP specimens analysed.

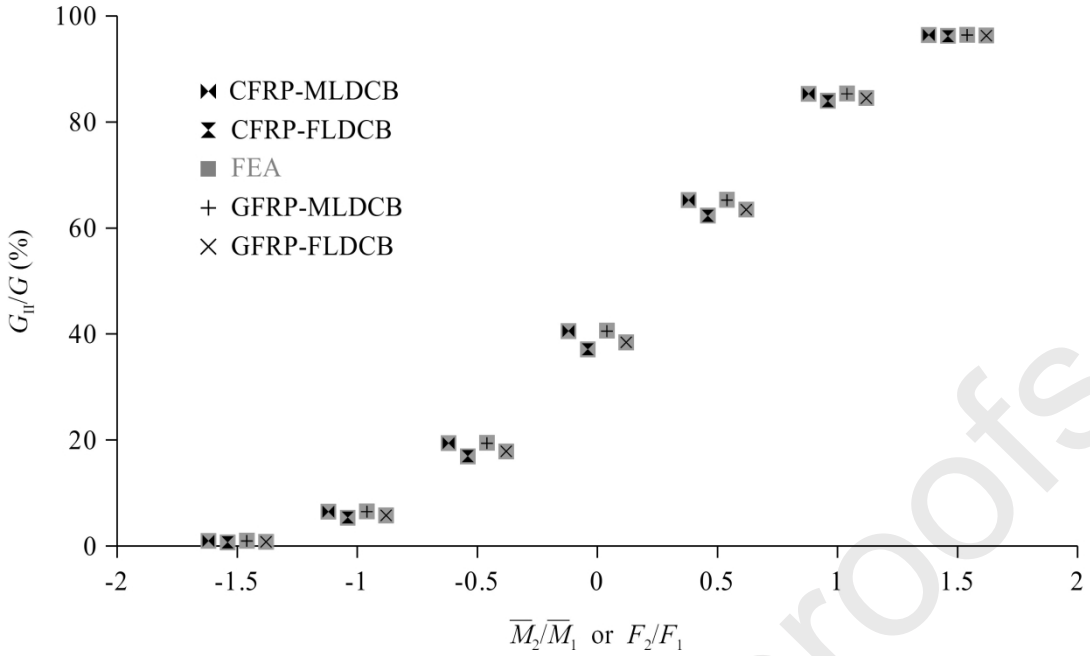

Fig. 5. Mode-mix ratio versus load ratio applied to MLDCB or FLDCB specimens (Fig. 1) with sub-laminate thickness ratio $h_2/h_1 = 1.5$. For clarity, the results were offset horizontally around the −1.5 to 1.5 scale load ratios.

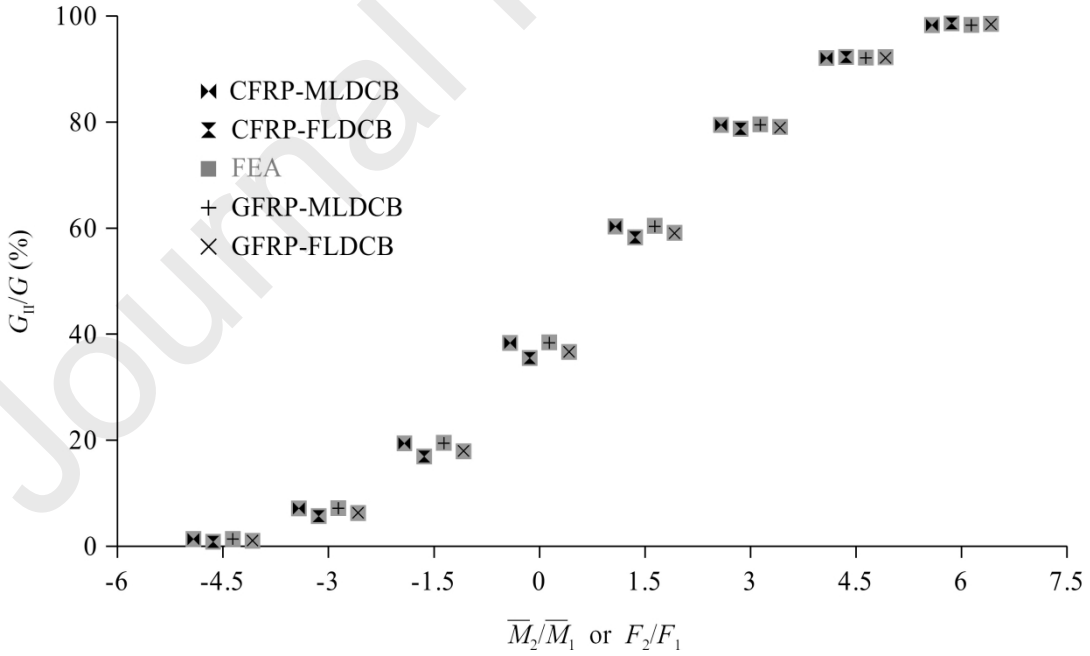

Fig. 6. Mode-mix ratio versus load ratio applied to MLDCB or FLDCB specimens (Fig. 1) with sub-laminate thickness ratio $h_2/h_1 = 3$. For clarity, the results were offset horizontally around the −4.5 to 6 scale load ratios.

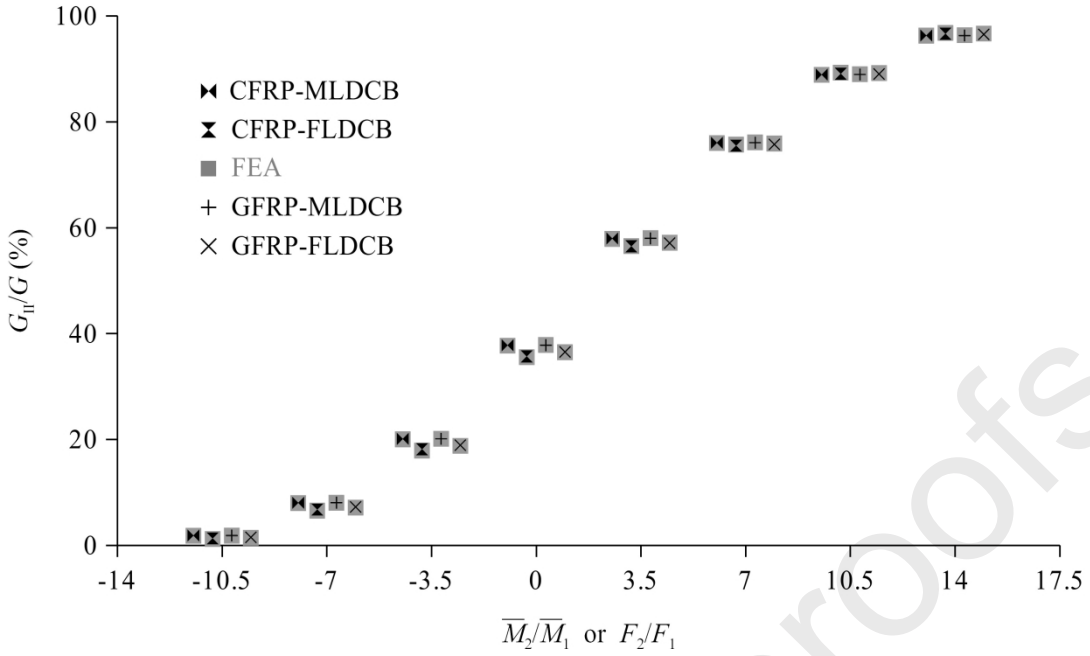

Fig. 7. Mode-mix ratio versus load ratio applied to MLDCB or FLDCB specimens (Fig. 1) with sub-laminate thickness ratio $h_2/h_1 = 5$. For clarity, the results were offset horizontally around the −10.5 to 14 scale load ratios.

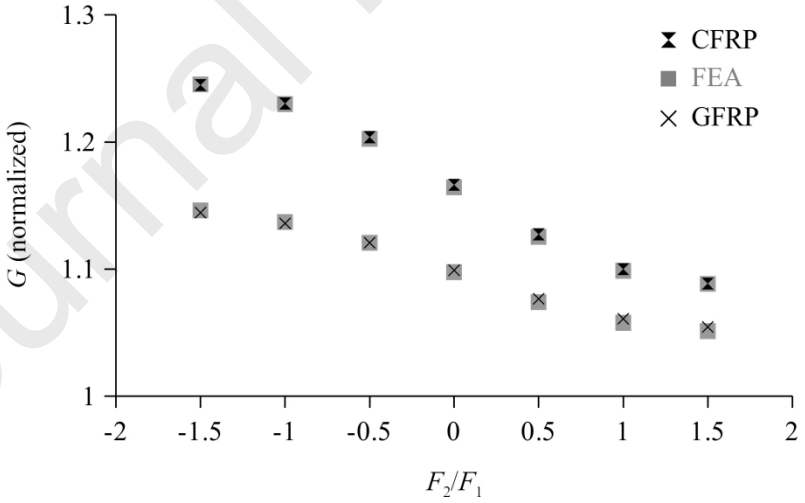

Fig. 8. Normalized strain-energy release rate versus force ratio applied to FLDCB specimens (Fig. 1) with sub-laminate thickness ratio $h_2/h_1 = 1.5$.

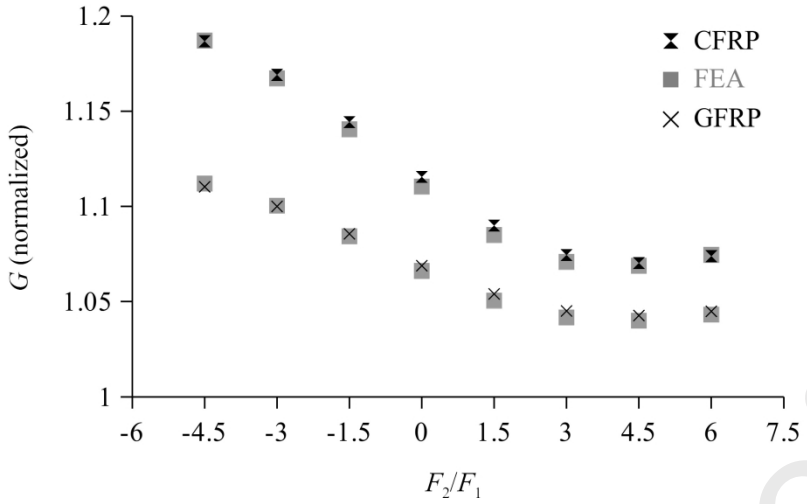

Fig. 9. Normalized strain-energy release rate versus force ratio applied to FLDCB specimens (Fig. 1) with sub-laminate thickness ratio $h_2/h_1 = 3$.

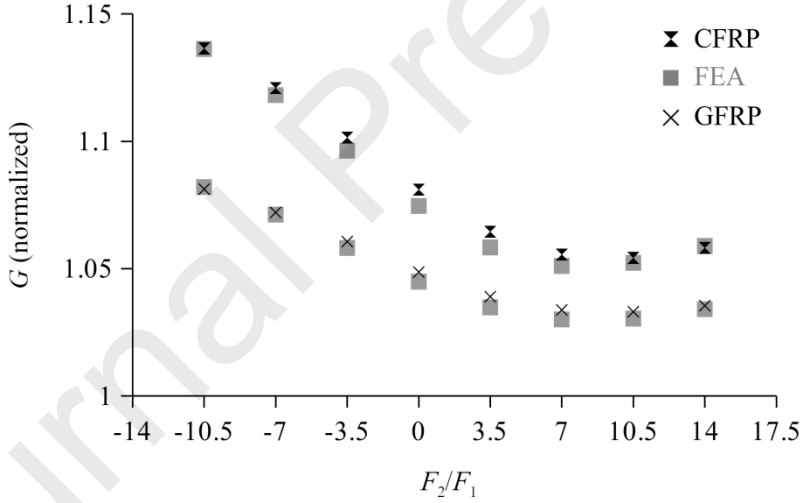

Fig.10. Normalized strain-energy release rate versus force ratio applied to FLDCB specimens (Fig. 1) with sub-laminate thickness ratio $h_2/h_1 = 5$.

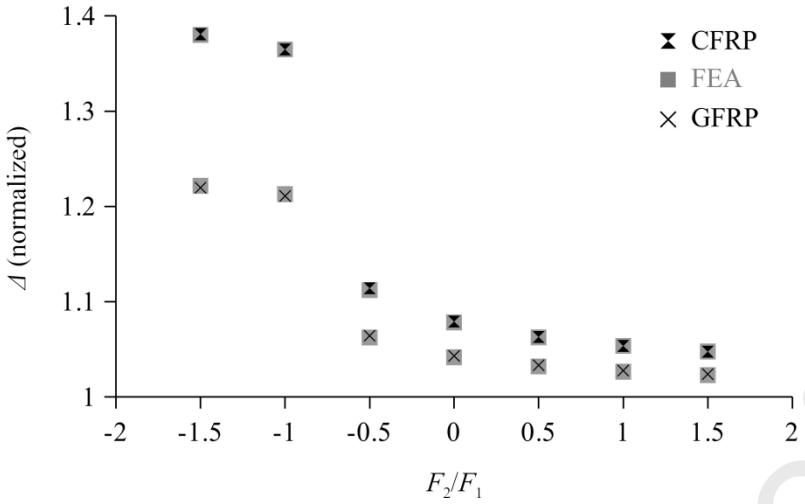

Fig. 11. Normalized vertical end-displacements Eq. (54) versus force ratio applied to FLDCB specimens (Fig. 1) with sub-laminate thickness ratio $h_2/h_1 = 1.5$.

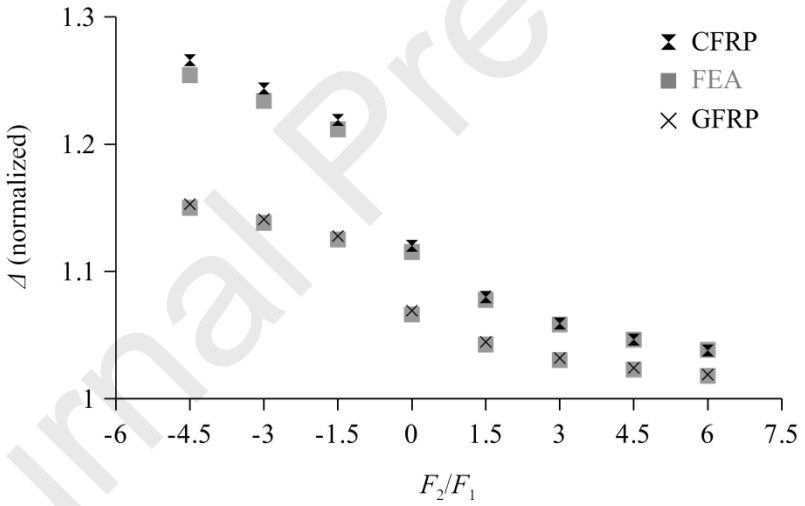

Fig. 12. Normalized vertical end-displacements Eq. (54) versus force ratio applied to FLDCB specimens (Fig. 1) with sub-laminate thickness ratio $h_2/h_1 = 3$.

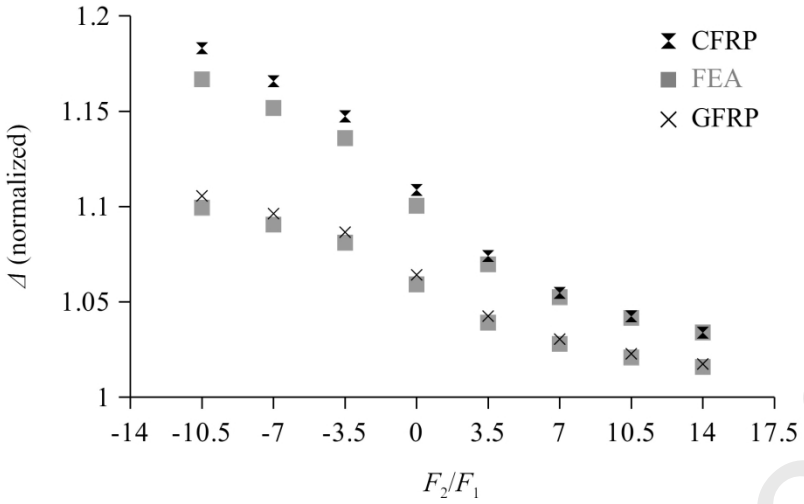

Fig. 13. Normalized vertical end-displacements Eq. (54) versus force ratio applied to FLDCB specimens (Fig. 1) with sub-laminate thickness ratio $h_2/h_1 = 5$.

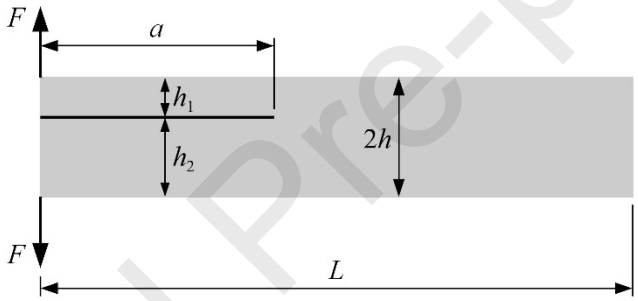

Fig. 14. The ADCB specimen.

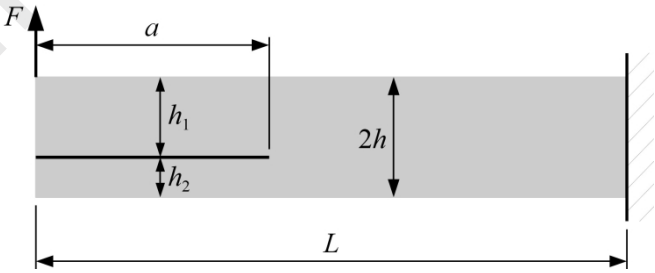

Fig. 15. The FRMM specimen.

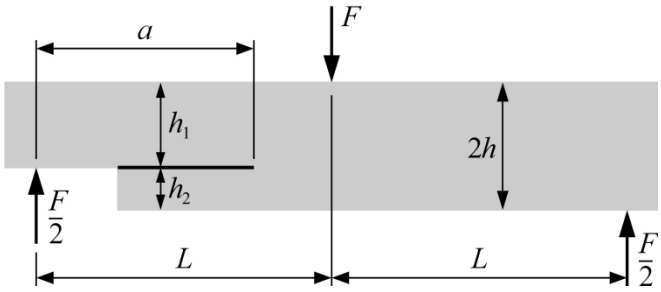

Fig. 16. The SLB specimen.

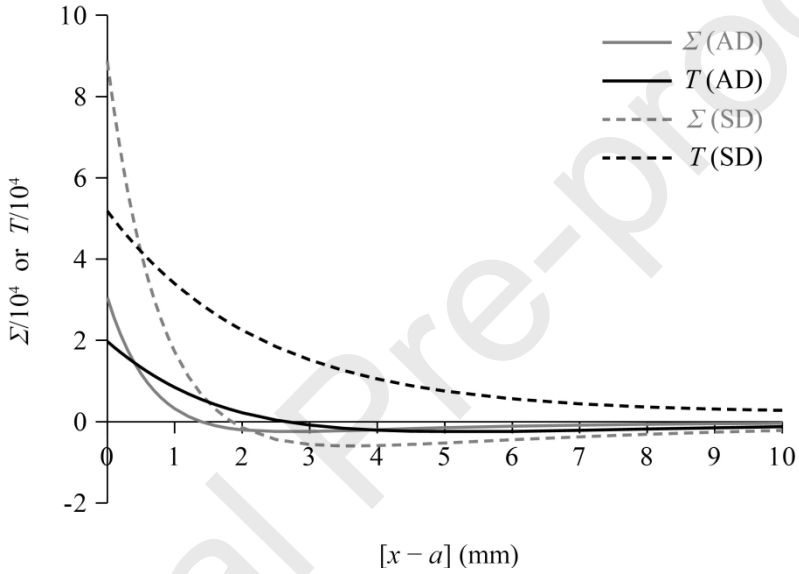

Fig. 17. Dimensionless tractions $\Sigma = b\sigma_c/G$ and $T = b\tau_c/G$ in asymmetrically (AD) and symmetrically delaminated (SD) specimens with $G_{II}/G = 22.5\%$.

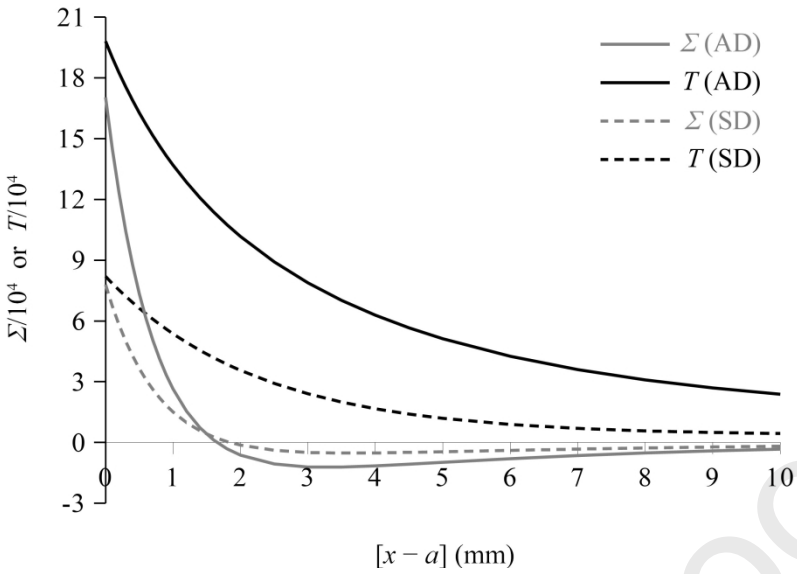

Fig. 18. Dimensionless tractions $\Sigma = b\sigma_c/G$ and $T = b\tau_c/G$ in asymmetrically (AD) and symmetrically delaminated (SD) specimens with G_{II}/G = 48.5%.

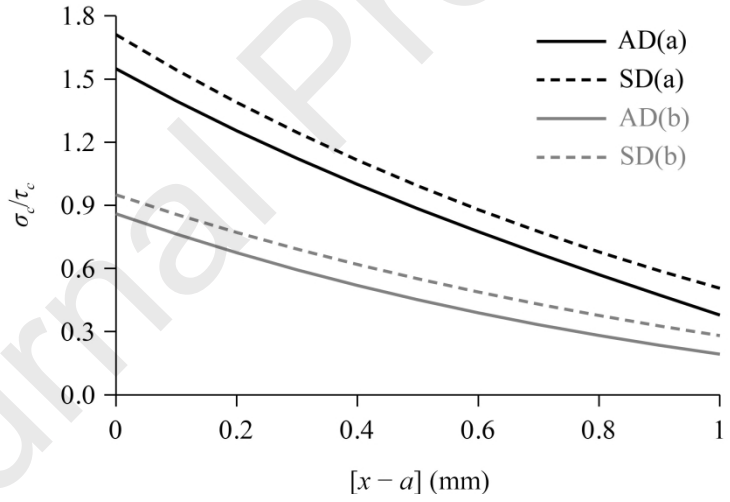

Fig. 19. Ratio of the tractions near the crack-tip for the asymmetrically (AD) and symmetrically delaminated (SD) specimens with G_{II}/G = 22.5% (a) and 48.5% (b).

Declaration of interests

☒ The authors declare that they have no known competing financial interests or personal relationships that could have appeared to influence the work reported in this paper.

☒The authors declare the following financial interests/personal relationships which may be considered as potential competing interests: